CHEMISTRY OF MATERIALS

Article

pubs.acs.org/cm

# Quantitative Analysis of the Morphology of {101} and {001} Faceted Anatase $TiO_2$ Nanocrystals and Its Implication on Photocatalytic Activity

Jue Liu,*[,†] Daniel Olds,[†] Rui Peng,[‡] Lei Yu,[§] Guo Shiou Foo,[‡] Shuo Qian,[#] Jong Keum,[‡] Beth S. Guiton,[§] Zili Wu,[‡] and Katharine Page*[,†]

[†]Chemical and Engineering Materials Division, Oak Ridge National Laboratory, Oak Ridge, Tennessee 37831, United States

[§]Department of Chemistry, University of Kentucky, Lexington, Kentucky 40506, United States

[‡]Center for Nanophase Materials Sciences, Oak Ridge National Laboratory, Oak Ridge, Tennessee 37831, United States

[#]Biology and Soft Matter Division, Oak Ridge National Laboratory, Oak Ridge, Tennessee 37831, United States

Supporting Information

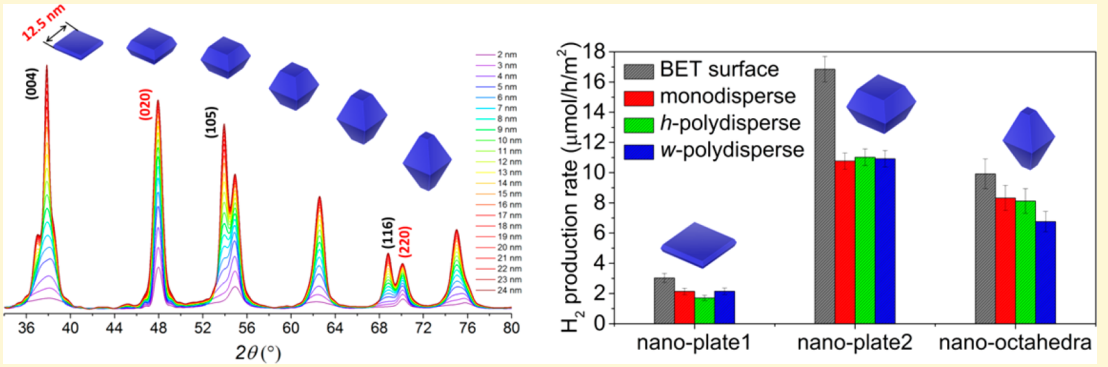


**ABSTRACT:** The atomistic structure and morphology (shape and size) of nanomaterials have strong influences on their physical and chemical properties. However, many characterization techniques focus exclusively on one length-scale regime or another when developing quantitative morphology/structural models. In this article, we demonstrate that powder X-ray diffraction and neutron pair distribution function (PDF) can be used to obtain accurate average morphology and atomistic structure of {001} and {101} faceted anatase $TiO_2$ nanocrystals based on differential evolution refinements using Debye scattering equation calculations. It is also demonstrated that the morphology polydispersity of $TiO_2$ nanocrystals can be effectively obtained from the diffraction data via a numerical refinement routine. The morphology refinement results are in good agreement with those from transmission electron microscopy and the modeling of small angle neutron scattering data. This method is successfully used to quantify the facet-specified photocatalytic hydrogen evolution activity of anatase $TiO_2$ nanocrystals with different {001} to {101} ratios. It is found that the sample with an intermediate amount of both {001} and {101} facets shows the best photocatalytic hydrogen evolution reaction (HER) activity. It is expected that the simultaneous structure and morphology refinement technique can be generally used to study the relationship between morphology and functionality of nanomaterials.

## INTRODUCTION

Nanomaterials have emerged as very important candidates for energy storage, catalysis, and semiconductor applications.[1−5] It has also been recognized for a long time that the morphology (particle shape and size) of nanomaterials can strongly affect their physical and chemical properties.[6−9] It is for this reason that nanomaterials with specific morphologies, such as nanospheres, -cubes, -octahedra, -plates, -needles, etc., are highly sought for a variety of applications.[10−14] Electron microscopy techniques, i.e., scanning electron microscopy (SEM) and transmission electron microscopy (TEM), as well as small-angle X-ray/neutron scattering (SANS/SAXS), have been widely used to investigate the morphologies of nanomaterials. However, it is worth noting that TEM and SEM images can only provide selected local morphology information, often conveying questionable representative results of the whole sample.[15,16] In addition, these approaches become problematic when nanoparticles are agglomerated,[17] and samples can be damaged by high energy electron beams.[18,19] Therefore, it is imperative to develop an average (bulk) morphology evaluation tool to assist traditional electron microscopy investigations to gain more reliable morphology information on nanomaterials.

Received: March 22, 2017
Revised: June 8, 2017
Published: June 14, 2017

ACS Publications © XXXX American Chemical Society



DOI: 10.1021/acs.chemmater.7b01172
Chem. Mater. XXXX, XXX, XXX−XXX

On the other hand, the composition and atomic structure also play a very important role for specific functionalities of nanomaterials. For example, the water splitting performance of $(ZnO)_x(GaN)_{1-x}$ nanoparticles is strongly correlated to its composition ($x$ value),[20] and the enhanced correlation of internal dipoles of $BaTiO_3$ nanocubes have been hypothesized to stabilize nanoscale ferroelectricity.[21] Therefore, to better understand the relationship between the functionality and structure of nanomaterials, it would be highly desirable to characterize the morphology and internal atomistic structure simultaneously.

X-ray or neutron Bragg diffraction has been widely used to gain accurate atomistic structures of crystalline materials.[22−24] This approach correlates the measured diffraction intensity with crystal structure by mathematical functions, notably the three Laue equations.[25,26] For large crystals, the translational periodicities along three crystallographic axis direction ($a$, $b$, and $c$) are large enough that each of these equations only differs from zero when Bragg diffraction conditions ($2d \sin\theta = n\lambda$) are strictly satisfied, and hence the Bragg diffraction peaks are very intense and sharp. In contrast, for small nanocrystals, the translational periodicities are limited or even eliminated and thus the nonzero areas broaden for the three Laue equations, resulting in much broader Bragg diffraction peaks: a phenomenon that is often termed as size broadening.[27,28] Therefore, measurement of the widths of Bragg diffraction peaks provides the simplest method to estimate the crystallite size of polycrystalline samples (depending on the instrumental resolution, sensitivity is typically available up to 100 nm in particle dimensions). Several well-adapted methods, such as the Scherrer equation,[27] Stokes−Wilson method,[29] and Warren−Averbach method,[30] can be used to treat the size broadening effects from powder diffraction data. However, it should be noted that the coexistence of strain, dislocations, or defects (e.g., stacking faults) may bring other isotropic or anisotropic broadening effects into the diffraction profiles. Theoretically, quantitative information about the atomistic structure and size of nanoparticles can be extracted from corresponding Bragg diffraction profiles if all of these broadening effects can be effectively deconvoluted.[31] However, in reality, Bragg diffraction peaks of small nanocrystals are often found to be so broad that they overlap significantly or even smear into the background, resulting in difficult profile deconvolution.[16,32] In addition, the existence of anisotropic particle shapes for many nanocrystals (e.g., nanodisks, -rods, -tetrapods) brings further complexity into the conventional Rietveld-type analysis. In contrast to the traditional treatment of powder diffraction data (in reciprocal space), the Debye scattering equation (DSE)[33] calculation operates in real space and takes no preassumption of any translational periodicity. Thus, it can be equally applied to materials with long-range order as well as materials with intermediate/short-range order or even amorphous materials and liquids.[34] Historically, the major limitation of using DSE for structure analysis is the requirement of tremendous amounts of computational power, as the summation of DSE runs over all atoms and thus the computational time is proportional to the square of the number of atoms in the particle ($\sim N^2$). However, as computational power continues to grow, the calculation of scattering profiles of nanoparticles with dimensions of tens of nanometers is now achievable within a reasonable amount of time (hours) even on personal computers. For example, several groups have successfully used the Debye scattering equation to study the morphology and atomistic structure of oxide nanoparticles[15,16,35] and lead chalcogenide quantum dots[36] with powder X-ray diffraction data.

Pair distribution function (PDF) analysis has emerged as another powerful tool to study the particle shape, size, and atomistic structure of nanomaterials or materials with appreciable amount of disorder.[34,37−40] The real-space-based PDF analysis utilizes both Bragg scattering and diffuse scattering information and thus is very sensitive to short-range ordering (SRO) in disordered materials or intermediate-range structure in nanoscale materials. Despite its great advantages in studying the structure of nanomaterials, it is worth noting that the detailed morphology (size and shape) information is often absent from the experimental PDF ($G(r)$) data due to the lack of low-$Q$ scattering data at dedicated PDF instruments (typical $Q_{min} \sim 0.1$ Å or higher), as can be seen in eq 1. This problem is overcome in modeling by implementing a characteristic shape function $\gamma_0(r)$, or the so-called envelope function, into the PDF analysis process.[41,42] However, this approach is effective only if a priori knowledge of the morphology (shape and size) of nanoparticles is obtained from other techniques such as TEM or small-angle X-ray/neutron scattering. More recently, our group developed a new approach for this "shape-correction" that can be used during structure refinement utilizing the calculated complete PDF $G^*(r)$ from an atomistic model with known $Q_{min}$ from measurements.[43] This approach provides an efficient route to quantitative analysis of the atomistic structure of nanomaterials using PDF data. This becomes even more critical in terms of irregular particle shapes where the calculation of accurate mathematical expressions for the shape function is exceptionally challenging.

$$\begin{aligned} G(r) &= \frac{2}{\pi}\int_{Q_{max}}^{Q_{min}} Q[S(Q) - 1]\sin(Qr)\,dQ \\ &= 4\pi r\rho(r) - 4\pi r\rho_0\gamma_0(r) \\ &= G^*(r) - 4\pi r\rho_0\gamma_0(r) \end{aligned} \quad (1)$$

In this article, we demonstrate that DSE analysis of Bragg diffraction and PDF can be used as a powerful tool to obtain accurate atomistic structure and morphology (shape, average particle size, and particle size distribution) information for {001} and {101} faceted anatase $TiO_2$ nanocrystals. Anatase $TiO_2$ nanocrystals have attracted tremendous attention in recent years because of their excellent catalytic, especially photocatalytic, activity.[5,44] In particular, $TiO_2$ nanocrystals with dominant {001} facets are highly desired because they are theoretically predicted to possess more active sites (five-coordinated Ti) and higher surface energy relative to other energetically more favorable facets such as {101} or {100} etc. and are thus believed to show better heterogeneous catalytic performance.[45,46] This assessment has been well adopted in the community for many years though very limited direct experimental evidence can be found, presumably due to the lack of high quality anatase $TiO_2$ samples with dominant {001} facets.[47] The tailored synthesis of {001} dominant nanocrystals had been found to be exceptionally challenging because the highly energetic {001} facets diminish quickly in equilibrium or near-equilibrium synthetic conditions.[46,48,49] Fortunately, Yang et al. discovered that {001} facets can be stabilized by using fluorine as a surface stabilizer under hydrothermal conditions.[7] Though the initial demonstration was to synthesize micrometer-sized $TiO_2$ single crystals with a high ratio of {001}


DOI: 10.1021/acs.chemmater.7b01172
Chem. Mater. XXXX, XXX, XXX−XXX

facets, this method was immediately adopted and modified to synthesize nanocrystals with larger surface areas for catalytic and energy storage related applications.[50,51] With tremendous successes in synthesizing anatase $TiO_2$ nanocrystals with different {001} ratios in recent years, more and more controversial experimental results about the ranking of the catalytic reactivity of different facets have been reported.[35,52] This controversy, in large part, is caused by the difficulty in separating the catalytic contribution from distinct facets and the lack of an effective method to accurately quantify the surface area of each facet.[35,53] This motivates us to carry out the current comprehensive morphology study of anatase $TiO_2$ nanocrystals with different amounts of {001} and {101} facets. By accurately determining the shape, size, and polydispersity of the synthesized nanocrystals, the relationship between the surface-normalized photocatalytic HER reactivity and the morphology of nanocrystals is successfully unraveled. This study also paves the way for quantitatively investigating the relationship between the functionality and the morphology of other technologically important nanomaterials based on the developed methods.

## EXPERIMENTAL DETAILS

**Synthesis of Anatase $TiO_2$ Nano-Octahedra and Nanoplates.** Aqueous $TiCl_4$ solution was prepared by adding 6.6 mL of $TiCl_4$ to 50 mL of aqueous HCl solution (0.43 mol/L) drop by drop under vigorous stirring in an ice bath. $TiCl_4$ solution was added to 5 wt % $NH_3{\cdot}H_2O$ aqueous solution drop by drop under vigorous stirring. After a light blue $Ti(OH)_4$ (precursor) precipitate was formed, 10 mL of 4 wt % aqueous $NH_3{\cdot}H_2O$ solution was added to adjust the pH between 6 and 7. The suspension was centrifuged after aging for 2 h at room temperature. The precipitate was washed two times with water and one time with ethanol. To prepare $TiO_2$ nano-octahedra, 2 g of fresh $Ti(OH)_4$ precursor was dispersed in 30 mL of 50 vol % water/isopropanol. The suspension was transferred to a 50 mL Teflon-lined autoclave and heated to 180 °C for 24 h. The product was centrifuged after the reaction and washed with deionized water three times and ethanol one time. $TiO_2$ nanoplates were prepared using $Ti(OC_4H_9)_4$ as precursor. $Ti(OC_4H_9)_4$ (5 mL) was added to 20 mL of distilled water drop by drop under stirring. A total of 0.5 mL of 47 wt % aqueous HF was added slowly after stirring for 15 min. The suspension was stirred for 30 min before being transferred to a 50 mL Teflon-lined autoclave and heated to 180 °C for 24 h. The product was centrifuged after the reaction and then extensively washed with NaOH solution to remove the surface F ligands.[35,54] The final product was then washed with ethanol three times before recovering. Both nano-octahedra and nanoplate samples were calcined at 300 °C for 4 h. To study the change in photocatalytic activity, another thicker nanoplate sample was synthesized by calcining the pristine nanoplates at 500 °C for 4 h. This is enabled by the nature of oriented attachment growth of these nanoplates in the *c*-axis direction at elevated temperatures (Figure S1,3).[55]

Brunauer–Emmett–Teller (BET) surface areas of the $TiO_2$ nanocrystals were measured via nitrogen adsorption at −196 °C using a Micrometrics Gemini 275 system. For the samples calcined at 300 °C, $TiO_2$ nanoplates and nano-octahedra have surface areas of 58 and 101 $m^2/g$, respectively. The thicker $TiO_2$ nanoplates calcined at 500 °C have a surface area of 36 $m^2/g$.

**X-ray Diffraction.** Powder diffraction patterns were collected on a PANalytical X'Pert MPD Pro X-ray powder diffractometer with Cu K$\alpha$ radiation ($\lambda$ = 1.54187 Å) equipped with an Anton Paar XRK-90 linear detector. The diffraction experiments were carried out with a step size of 0.016711° and at a scan rate of 80 s/step in Bragg–Brentano configuration. The primary and secondary radius was set to 240 mm. Le Bail and Rietveld analyses were carried out in the TOPAS software suite (version 6). Simulations of corresponding powder diffraction patterns using the Debye scattering equation were conducted in the DISCUS/KUPLOT/DIFFEV program suite.[56] The instrumental function is modeled with a symmetrical Pseudo-Voigt function obtained from fitting the diffraction profile of a standard $CeO_2$ powder specimen.

**Neutron Pair Distribution Function.** Neutron total scattering data were collected at the NOMAD beamline at the Spallation Neutron Source (SNS) at Oak Ridge National Laboratory. NOMAD is a high flux, intermediate resolution neutron powder diffractometer that is specifically designed for high quality neutron total scattering (both Bragg scattering and diffuse scattering). For the current experiment, about 0.2–0.3 g of powder samples were loaded into 3 mm quartz capillaries. Two 30 min scans were collected for each powder sample and then summed together to improve the statistics. The detectors were calibrated using scattering from a diamond powder standard prior to the measurements. Neutron powder diffraction data were normalized against a vanadium rod, the background was subtracted, and the total scattering structure factor $S(Q)$ data were transformed to pair distribution function data $G(r)$ using the specific IDL codes developed for the NOMAD instrument.[57] Small box (unit-cell based) refinements were carried out in the TOPAS software suite (version 6).[58] Further particle morphology simulations/refinements were carried out in the DISCUS/KUPLOT/DIFFEV software package.[48]

**Small Angle Neutron Scattering.** Small angle neutron scattering (SANS) data were collected at the Bio-SANS beamline at the High Flux Isotope Reactor (HFIR) at Oak Ridge National Laboratory.[59] Bio-SANS is a moderate resolution, broad *Q*-range small angle instrument optimized for the study of complex and hierarchical structures across multiple length scales. The neutron wavelength was 6 Å with wavelength spread ∼13.2%. Two position sensitive detectors covering low-*Q* and high-*Q* respectively were configured to provide a *Q* coverage of 0.007–0.9 $Å^{-1}$ for the measurement. A powder sample of $TiO_2$ nanoplates held in 3 mm quartz capillaries was measured at room temperature. The SANS data were reduced and azimuthally averaged using standard procedures to correct for detector sensitivity, instrument dark current, sample transmission, and quartz capillary background with facility-provided data reduction software Mantid.[60] Data were fit using the size distribution module of the Irena macros for Igor Pro,[61] modeling the structure as a disc with thickness 9.7 nm. Using Moore's indirect Fourier transform method,[62] the pair–distance distribution function was calculated from the data, corresponding to the total scattering $G(r)$. Small angle scattering profiles were calculated for the atomistic models[63] fit within the DISCUS/KUPLOT/DIFFEV refinements, which were then weighted and combined using polydispersity profiles derived from the diffraction fits. Additionally, the product of two derived polydispersity profiles (varying both width and height) was computed.

**Transmission Electron Microscopy (TEM).** TEM imaging was performed on a Hitachi HF-3300 at 300 kV. TEM samples were prepared by sonication of the as-synthesized anatase $TiO_2$ nanoplates and nano-octahedra in isopropanol, followed by dropcasting onto the lacey carbon coated copper TEM grids and then drying at 60 °C for 1 h. Manual counting was used to analyze the width and thickness dispersion of nanoplates from TEM images in ImageJ.[64]

**Hydrogen Evolution Reaction (HER) Activity.** Photocatalytic hydrogen evolution reaction over the $TiO_2$ samples was carried out in a quartz reactor. In a typical photocatalytic experiment, 40 mg of $TiO_2$ was dispersed via sonication in 40 mL of water/methanol (3:1 volume ratio) solution. Prior to the photocatalytic reaction, the quartz cell was deaerated by a continuous flush with ultrahigh pure Argon gas for 30 min. The light input is provided by a 200-W Hg lamp equipped with a band-pass filter to allow the pass of UV light with wavelength in the range of 325–385 nm. The suspension was stirred vigorously during the entire photocatalytic reaction, and the temperature of the system was held at 25 °C by the cooling water circulating around the entire quartz cell. The hydrogen gas yield was determined and quantified by using gas chromatography compiled with a hydrogen calibration plot, with model BUCK 910 (molecular sieve column, TCD detector, and Argon as carrier gas). To calculate the apparent quantum yield (AQY), we used the average 355 nm for the UV light source. The energy of photon is $E_{ph} = h\nu = hc/\lambda$, where $h$ is the Planck's constant, $\nu$ is the


DOI: 10.1021/acs.chemmater.7b01172
Chem. Mater. XXXX, XXX, XXX–XXX

frequency, $c$ is the speed of light, and $\lambda$ is the wavelength of the light source. Therefore, the energy of photon for solar simulated light source is determined to be $5.6 \times 10^{-19}$ J. The number of the photons irradiating per second on the reactor can be calculated by equation $N_{ph} = \Phi/E_{ph}$, where $\Phi$ is the intensity of the light source hitting on quartz reactor (it was measured to be 8.8 W by a Newport 843-R power meter). The number of electrons that are effectively participated in the photocatalytic reaction can be determined from the hydrogen yield and are determined by equation $N_e$ = (hydrogen yield per hour) × 2 × (Avogadro's number), where hydrogen yield per hour is calculated by using the hydrogen yield divided by the corresponding number of hours. Taking everything together, the AQY is determined as $(N_e/N_{ph}/3600) \times 100\%$.

## RESULTS AND DISCUSSION

**Qualitative Morphology Analysis.** According to the theoretical calculation of Barnard et al.,[65] anatase $TiO_2$ nanocrystals with slightly truncated octahedral (or tetragonal bipyramid) shape (those with dominant {101} facets) are predicted to possess the lowest surface energy under hydrogenated or hydroxyl conditions. This is fully consistent with experimental observations of the morphology of synthetic and natural anatase $TiO_2$.[47] To synthesize nanocrystals with dominant highly energetic {001} facets, it is necessary to modify the relative surface energy between (001) and (101) faces. One effective method is to partially replace the surface oxygen or hydroxyl by capping ligands with stronger electronegativity, such as fluorine, during the synthetic process.[7] In the current study, anatase $TiO_2$ nanocrystals with two different morphologies were successfully synthesized using hydrothermal reaction with and without hydrofluoric acid (HF) agent. TEM images (Figures S1 and S2) confirm that the sample synthesized without HF is dominated by slightly truncated nano-octahedra with dominant {101} facets while the one synthesized with HF contains a majority of thin nanoplates with a high percentage of {001} facets. A third sample of thicker nanoplates with an intermediate amount of {001} and {101} facets was synthesized by calcining the {001} dominant nanoplates at 500 °C for 4 h (Figure S3). It is worth noting that these hydrothermally synthesized samples are highly agglomerated, making accurate morphology analysis difficult using automatic TEM counting or small angle scattering approaches.

Powder X-ray (Cu K$\alpha$) diffraction patterns of these two samples (300 °C nanoplates and nano-octahedra) are remarkably different, as can be seen in Figure S4. The diffraction pattern of the truncated nano-octahedra sample shows no obvious anisotropic peak broadening, indicating the near isotropic morphology (slightly truncated octahedra) of this sample. In clear contrast, the diffraction pattern of the nanoplate sample shows strong anisotropic peak broadening with much weaker and broader 004, 105, and 116 reflections relative to reflections associated with *ab*-plane dimensions such as 020 (or 200) and 220. This feature indicates that the as-prepared nanocrystals are highly anisotropic with much larger coherence length within *ab*-plane dimensions and very limited coherence length along the *c*-axis direction. These observations suggest that two parameters, the plate width ($w$) and thickness ($h$), are required to describe the morphology of the as-prepared anatase $TiO_2$ nanocrystals. It is worthwhile to note that strain/dislocation may also contribute to the broadening of Bragg diffraction peaks, yet the fwhm (full width at half-maximum) of the diffraction peaks associated with the *c*-axis direction or *ab*-plane dimension are nearly proportional to $1/\cos\theta$ and thus indicate that size broadening is the dominant effect for peak broadening (Figure S5).[66] Therefore, no strain or dislocation induced effects will be considered in the current report. In addition, since X-rays are not sensitive to light atoms and H mainly contributes to the incoherent scattering in the neutron scattering data, the intensity contributions from residual surface ligands, such as −OH or −H, will also be ignored for the current study.

We first carried out sensitivity tests to prove that the Debye scattering equation (DSE) calculation of powder X-ray diffraction data can be used as an effective tool to probe the average morphology of {101} and {001} faceted nanocrystals. For the sensitivity test of thickness ($h$), a series of truncated anatase $TiO_2$ nano-octahera with fixed *ab*-plane width (12.5 nm) but variable thickness (from 2 to 24 nm with a step size of 1 nm) were created using DISCUS software.[56] The $TiO_2$ anatase unit cell was expanded to a 40 × 40 × 30 supercell and then truncated into the desired morphology with specific boundary conditions. The simulated XRD patterns using DSE calculation are shown in Figure 1a, clearly showing that the relative peak intensity of 004, 105, and 116 reflections increases as the thickness increases. In addition, the Bragg diffraction peaks become sharper and more symmetric as the thickness increases. These simulations indicate that powder XRD is indeed highly sensitive to the variation of the thickness of

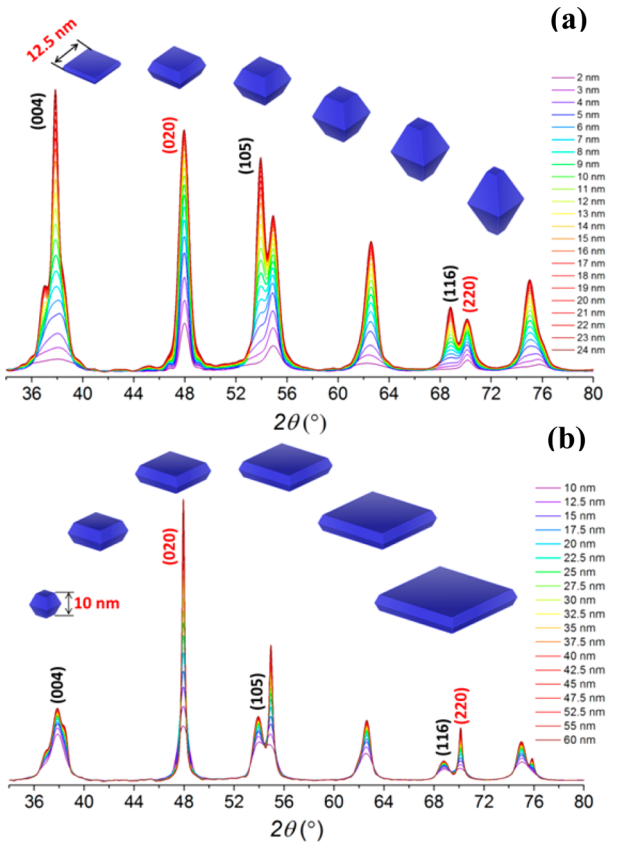


**Figure 1.** Simulated X-ray ($\lambda$ = 1.54187 Å) diffraction patterns of truncated anatase $TiO_2$ nanocrystals with (a) fixed *ab*-plane width (12.5 nm) as a function of thickness along the *c*-axis direction and (b) fixed thickness (10 nm) as a function of *ab*-plane width. Note a limited $2\theta$-range is shown. The red colored *hkl* indices are the reflections associated with *ab*-plane dimensions while the black indices are the reflections with major contributions from the *c*-axis direction.


DOI: 10.1021/acs.chemmater.7b01172
Chem. Mater. XXXX, XXX, XXX−XXX

nanoplates up to approximately 20 nm thickness, beyond which patterns become difficult to distinguish. Sensitivity tests of the *ab*-plane ($w$) dimensions were carried out in a similar manner: the thicknesses of truncated nano-octahedra were fixed to 10 nm while the plate widths were varied from 10 to 60 nm with a step size of 2.5 nm. The simulated XRD patterns (Figure 1b) reveal that the reflections associated with in *ab*-plane scattering such as 020 and 220 become sharper and more intense as the plate width increases, up to approximately 50 nm, above which the patterns appear very similar. In contrast, 004, 105, and 116 reflections remain relatively broad with only subtle intensity increases. Overall, the powder XRD is likely to be very sensitive to the average morphology ($h$ and $w$) of {101} and {001} faceted anatase $TiO_2$ nanocrystals in this size regime.

These results inspired us to further estimate the morphology of these two different faceted nanocrystals by visually comparing the DSE simulated X-ray diffraction data to the experimental data. By varying the width ($w$) and thickness ($h$) of the truncated nano-octahedra, a reasonable agreement between simulated patterns (blue curves) and background corrected experimental data (red curves) has been achieved for both samples, as can be seen in Figure 2. The $TiO_2$ nanocrystals synthesized without HF are found to be slightly truncated nano-octahedra with an estimated $w$ of 12.5 nm and $h$ of 18 nm, while the ones synthesized with HF agent are more heavily truncated with larger plate width $w$ of 35 nm and much thinner $h$ of 10 nm. This result is in good agreement with previous theoretical calculations and experimental observations[7,50] and also matches our TEM observations (Figures S1 and S2). However, it is worth noting that the relative intensity of some diffraction peaks, such as the 101 reflection, of simulated diffraction patterns are much stronger than the experimental data, indicating that quantitative refinement of both atomistic structure and morphology is needed.

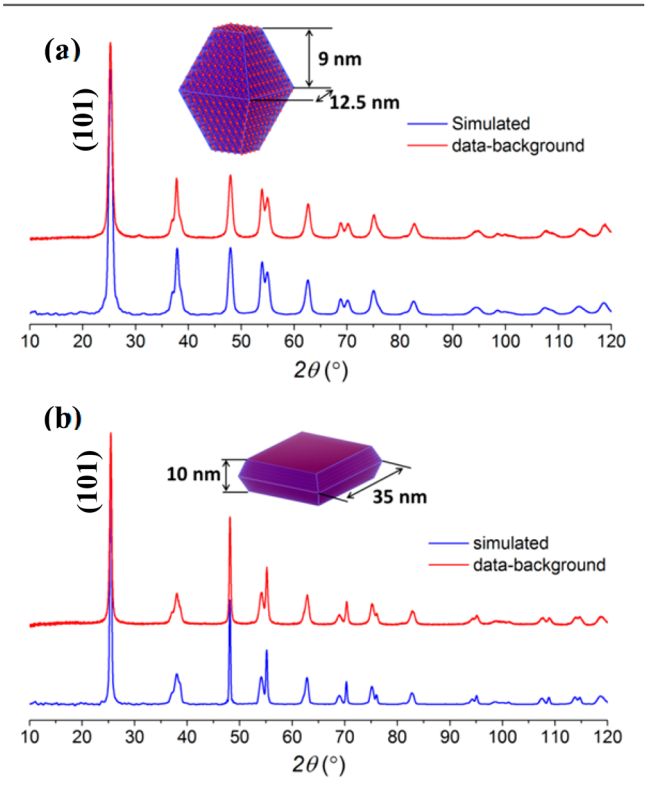


**Figure 2.** (a) Simulated X-ray diffraction ($\lambda$ = 1.54187 Å) pattern (blue) of $TiO_2$ nano-octahedra with dimensions of 12.5 nm ($w$) by 9 nm ($h$). For comparison, experimental X-ray (Cu K$\alpha$) diffraction data with background subtraction is shown in red. (b) Simulated X-ray diffraction ($\lambda$ = 1.54187 Å) pattern (blue) of $TiO_2$ nanoplate with dimensions of 10 nm (*ab*-plane width) by 35 nm (thickness), shown with experimental diffraction data in red.

Morphology sensitivity analysis using neutron pair distribution function calculation was carried out in a similar fashion as that for the powder X-ray diffraction. However, it is worth noting that the reduced pair distribution function is computed from the Fourier transformation of the normalized scattering intensity (eq 1); thus, the theoretical reduced pair distribution function $G^*(r)$ can be obtained only if the full $Q$-range of scattering data is available, which is experimentally unachievable. The lack of low-$Q$ data gives rise to a characteristic difference between the experimental $G(r)$ and the theoretical $G^*(r)$ pertaining to long length-scale structural features, often referred to as the particle shape function. In the current study, an empirical method was used to extract the shape function out of the theoretical $G^*(r)$ through an inverse deconvolution routine, and details about the methodology can be found in the report by Olds et al.[43] Moreover, instrumental resolution, which is often expressed as the dampening effect ($e^{-1/2(Q_{damp}/r)^2}$), strongly affects the sensitivity of PDF data at long pair−pair distances ($r$). For a moderate or high resolution PDF instrument such as NOMAD (with $Q_{damp}$ between 0.01 and 0.02 Å), the $G(r)$ intensity will smear out at pair−pair distance larger than 200 Å, making it difficult to gain reliable morphology information on nanomaterials with an average particle size larger than 20 nm. To demonstrate the sensitivity of using neutron PDF to determine nanoplate thickness ($h$), a series of theoretical $G^*(r)$ were calculated from truncated anatase $TiO_2$ nano-octahedra with variable thickness but fixed width ($w$ = 12.5 nm) in DISCUS,[56] and the dampening effect ($Q_{damp}$ = 0.0180 Å) was fixed to the value obtained from refinement of a standard Si sample measured on NOMAD. Shape-corrected $G(r)$ data were then calculated using Dshaper.[43] The extracted shape functions and a selected region of shape-corrected PDF data (40 Å to 60 Å) are shown in Figure 3a,b. It clearly shows that the simulated PDFs and shape functions are indeed very sensitive to the thickness variation up to about 14 nm. The intensity change becomes subtle above this value. Similar calculations were carried out to test the sensitivity of plate width ($w$). Corresponding shape function and corrected PDF data are shown in Figure 3c,d. It can be seen that, with fixed thickness (10 nm), the calculated patterns are sensitive to the width variation up to about 30 nm. It is also worth noting that the simulated PDF data in the range of several unit cells (Figures S6a and S7a, 0−20 Å) are essentially the same for nanocrystals with either different thickness or different width in this size regime (particle sizes over 10 nm); the differences in $G(r)$ becomes observable only at atomic pair−pair distances larger than 20 Å. Thus, collecting high resolution experimental $G(r)$ with small dampening effect is crucial for the accurate determination of the morphology of these anatase $TiO_2$ nanocrystals.

**Quantitative Morphology Refinement for Nano-Octahedra with a Monodisperse Morphology Model.** Regular Rietveld refinement with powder XRD was carried out for $TiO_2$ nano-octahedra using the fundamental parameter approach[67] with isotropic (spherical) particle shape. The refinement result is shown in Figure 4a and Table S1. A


DOI: 10.1021/acs.chemmater.7b01172
Chem. Mater. XXXX, XXX, XXX−XXX

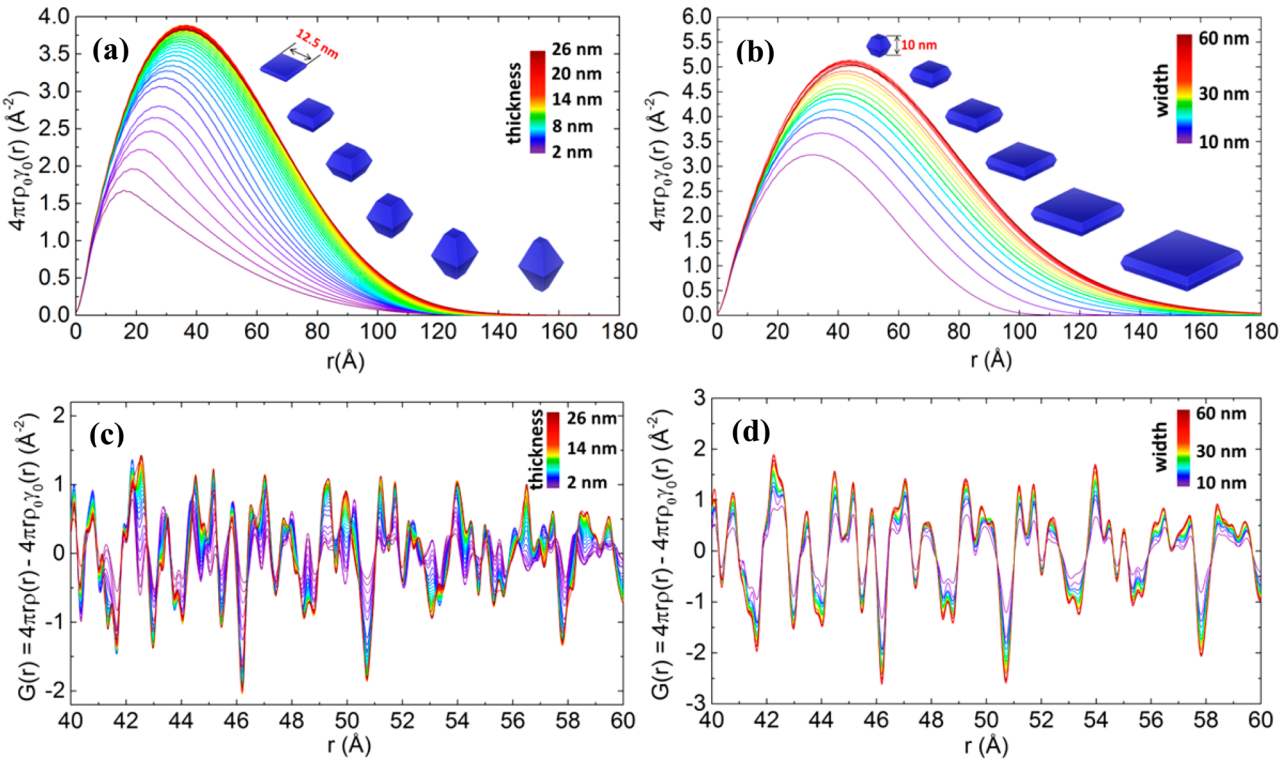


**Figure 3.** Simulated shape functions for truncated $TiO_2$ nanocrystals with (a) variable thickness (2 to 26 nm) but fixed width (12.5 nm) and (b) with variable width (10 to 60 nm) but fixed thickness (10 nm). Corresponding shape-corrected neutron PDF data (40 Å to 60 Å) are shown in (c) and (d) separately. Note that shape functions and PDF data have been calculated taking the instrument resolution effects expected at the NOMAD instrument into account.

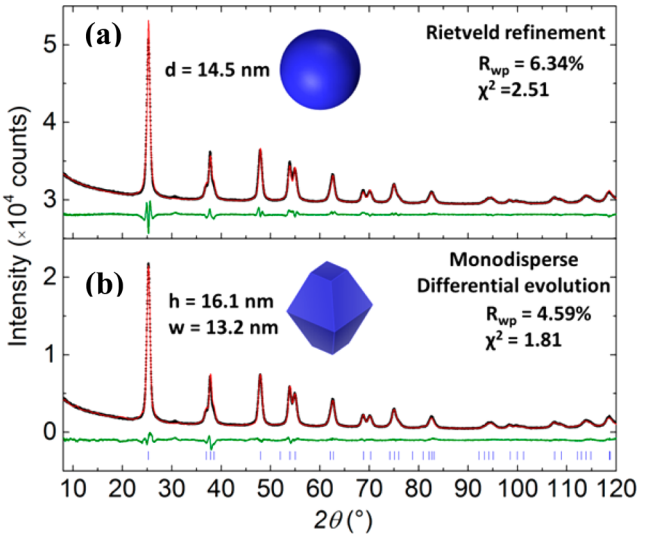


**Figure 4.** (a) Rietveld refinement of $TiO_2$ nano-octahedra against powder X-ray diffraction data (Cu K$\alpha$ radiation) using a $TiO_2$ bulk structure model with isotropic size broadening. (b) Structure and morphology refinement using combined differential evolution and least-squares refinement with Debye scattering equation calculation. Experimental data are shown as black dots, calculated pattern in red, tick marks indicating Bragg reflections in blue, and difference curve in green. The refined average morphologies are inserted.

reasonable agreement between the calculated pattern and experimental data has been achieved. However, intensity mismatch for the 101 ($2\theta$ around 25°) and 200 ($2\theta$ around 48°) reflections can be observed in the difference curve, which is very likely caused by the slightly anisotropic particle shape. In addition, the refined atomic displacement parameters for Ti and O are negative, indicating that thermal vibration induced intensity dampening tends to compensate for the anisotropic morphology induced intensity variation. This result indicates that quantitative morphology modeling is critical for accurate atomistic structure refinement of the as-prepared $TiO_2$ nanocrystals.

One of the greatest advantages of DSE refinement is that, theoretically, atomistic structure and morphology information can be simultaneously refined from the same data set (e.g., Bragg diffraction data or PDF). Unfortunately, the conventional least-squares minimization algorithm, which is computationally effective, cannot be directly used for the DSE refinement because of the discrete functional dependence between refinement criteria ($R$ values or $\chi^2$) and morphology-dependent variables ($w$ and $h$ here). Therefore, most reported DSE analyses are limited to qualitative simulations.[68] More recently, global minimization techniques, such as simulated annealing[16] and differential evolution algorithms,[15] have been successfully implemented into the DSE refinement. However, these refinement algorithms are much slower relative to the gradient least-squares minimization, further slowing the already computationally expensive DSE calculation. In a differential evolution refinement, a model progresses with a population of candidate structures. The characteristics (parameters) of the population members are evaluated against data and ranked before generating parameters for the next generation of candidate models. Since there is a whole population of structures to evaluate, it is highly desirable to limit the number of free parameters used for the global optimization. In the current study, only the structure and morphology related


DOI: 10.1021/acs.chemmater.7b01172
Chem. Mater. XXXX, XXX, XXX−XXX

parameters, namely, lattice parameter $a$ and $c$, atomic displacements of Ti and O, $z$-axis coordinate of O, the size in the $ab$-plane ($w$), and the size along the $c$-axis direction ($h$), are refined via the evolution algorithm (a brief introduction of the differential evolution algorithm can be found in the Supporting Information and related references[69]), while other parameters such as a scale factor and background functions are refined using least-squares minimization. A detailed refinement scheme is shown in Figure S8. The structure of bulk anatase $TiO_2$ was used as an initial model with an estimated starting $w$ of 12.5 nm and $h$ of 18 nm. Detailed refinement routines and boundary conditions of structural parameters can be found in the Supporting Information.

Remarkably good agreement ($R_{wp} \sim 4.50\%$) between the simulated and experimental data was reached after 350 refinement generations. However, a careful inspection of the $R_{wp}$ values for all 60 members (the population used for differential evolution refinement) reveals that the refinement did not converge after 350 generations. Instead, it splits into two different groups, as can be seen in Figure S9. This result is highly informative, which indicates that strong correlation exists among some of the refined parameters. Indeed, the atomic displacement of Ti ($B_{Ti}$) and O ($B_O$) is found to be strongly correlated with the morphology parameters ($h$ and $w$). Therefore, the atomic displacement parameters of Ti and O were fixed to the values ($B_{Ti}$ = 0.45 Å$^2$ and $B_O$ = 0.85 Å$^2$) obtained from refinement of PDF data (details can be found in the next paragraph). The final refinement result is shown in Figure 4b; an excellent fit has been achieved with $R_{wp}$ = 4.59% and $\chi^2$ = 1.81. The evolution of refined parameters can be found in Figure 5 and Figure S10. The final refined structure and morphology information are shown in Table 1. The average width in the $ab$-plane was refined to be 13.4(5) nm, and the thickness was refined to be 16.4(8) nm. These values differ dramatically from the qualitative estimation where width is estimated to be 12.5 nm and thickness is estimated to be 18.0 nm. This result suggests that simultaneous atomistic structure and morphology refinement is critical for accurate morphology quantification.

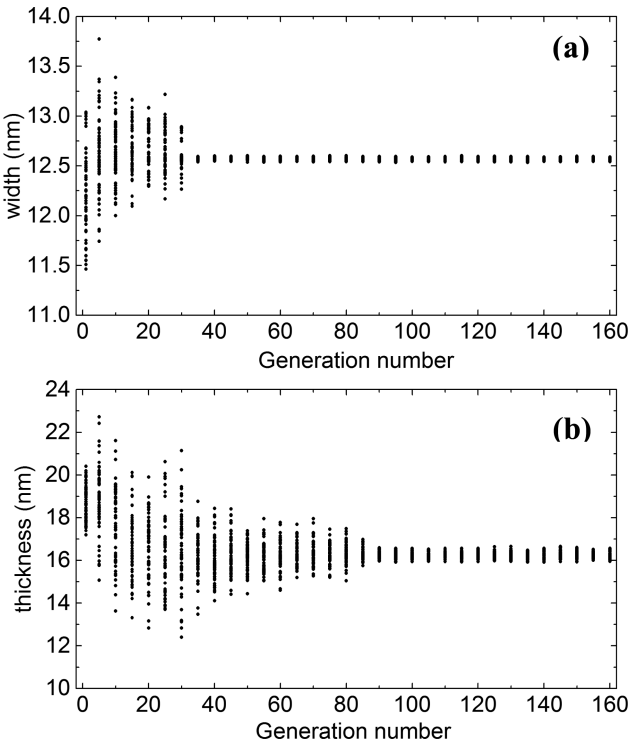


**Figure 5.** Evolution of width (a) and thickness (b) parameters in the population set as a function of refinement generation using differential evolution refinement with XRD data. It can be seen that the width of the plate converges to around 13.4 nm while the thickness converges to about 16.4 nm.

**Table 1. Atomistic Structure and Morphology of {101} Dominant Nano-Octahedra Refined from Powder XRD Data Using the Combined Differential Evolution and Least-Square Minimization with the Monodisperse Model[a]**

| atom | Wyck. | $x$ | $y$ | $z$ | occ. | $B_{iso}$ (Å$^2$) |
|---|---|---|---|---|---|---|
| Ti | 2a | 0.00 | 0.25 | 0.375 | 1.0 | 0.45 |
| O | 4f | 0.00 | 0.25 | 0.1688(4) | 1.0 | 0.85 |

[a]Width ($w$) = 13.4 (5) nm; thickness ($h$) = 16.4 (8) nm. S.G. $I4_1/amd$; $a$ = 3.7866 (1) Å; $c$ = 9.4990 (1) Å.

A similar strategy was used for the structure and morphology refinement using neutron PDF data. Noticeable improvement was achieved for the fit with differential evolution refinement relative to that of the conventional least-squares refinement, as can be seen in Figure 6. The refined structure and morphology information are listed in Table S2, and the evolution of structural parameters during refinement is shown in Figure S11. Results are consistent, though far more quantitative, than observations from TEM images in Figure S2. In contrast to the refinement using XRD data, no obvious correlation between $B_{Ti}$ and $B_O$ is observed, reflecting the importance of incorporating neutron total scattering into the structural analysis. In both the XRD and the neutron PDF cases, data is better fit and models are more reasonable with refinement strategies incorporating particle shape. Interestingly, refined $h$ and $w$ parameters were found equivalent within error in the XRD and neutron PDF analyses, though the atomic displacement parameters had to be

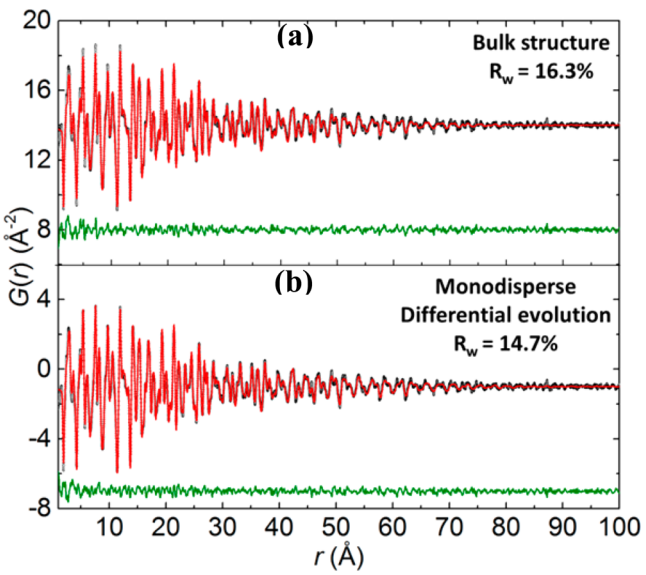


**Figure 6.** Result of least-squares refinement (a) versus differential evolution and (b) using neutron pair distribution function. Data are shown as black circles, model fits as red lines, and difference curves as green lines offset below the data and model fit.


DOI: 10.1021/acs.chemmater.7b01172
Chem. Mater. XXXX, XXX, XXX−XXX

fixed in the XRD data to neutron PDF determined values. In general, it is expected that the PDF will be more sensitive to smaller nanoparticles (<20 nm dimensions) while diffraction data will be more sensitive to larger nanoparticles (with an upper limit of sensitivity that depends on the instrument resolution).

**Quantitative Morphology Refinement for $TiO_2$ Nanoplates (300 °C) with a Monodisperse Morphology Model.** Rietveld refinement with bulk anatase $TiO_2$ structure using XRD data of nanoplates was performed in a similar manner as that for the nano-octahedra. The results are shown in Figure 7a and Table S3. The fit is significantly worse than

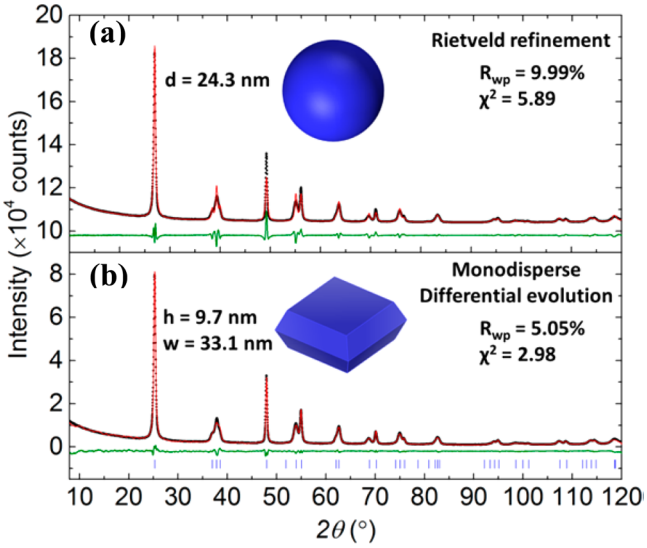


**Figure 7.** Rietveld refinement (a) versus differential evolution refinement and (b) against XRD data (fixed $B_{iso}$ values and atomic positions) for $TiO_2$ nanoplates. Experimental data are shown as black dots, calculated pattern in red, tick marks indicating Bragg reflections in blue, and difference curve in green. The refined morphologies are inserted.

that of the Rietveld refinement of the nano-octahedra sample due to the more anisotropic particle shape of these heavily truncated thin nanoplates. It is also worth noting that the atomic displacements of Ti and O refine to negative values, indicating that the atomic structure parameters cannot be accurately determined without quantifying the particle morphology. This inspires us to carry out the simultaneous atomistic structure and morphology refinement using the global minimization algorithm. However, since the particle size of these nanoplates is large enough (~35 × 35 nm in the *ab*-plane) to prevent fast DSE calculation,[16] it is prohibitive to refine all structure and morphology parameters at the same time. In order to confine the refinement to a reasonably achievable time, only the morphology related parameters ($w$ and $h$) and lattice parameters ($a$ and $c$) were refined via the differential evolution method, while the $z$-axis coordinate of O ($z$ = 0.1688) and the atomic displacements were fixed to the values from the previous refinement of nano-octahedra ($B_{Ti}$ = 0.45 Å$^2$ and $B_O$ = 0.85 Å$^2$). It can be seen from Figure 7 that remarkable improvements have been achieved from the differential evolution refinement relative to that from the Rietveld refinement. The weighted refinement residual drops from 9.99% (Rietveld refinement) to 5.05% (differential evolution refinement) after 50 generations.

The evolution of parameters during refinement is shown in Figure S12. The average width is refined to be 33.1(8) nm, and thickness is refined to be 9.7(3) nm. These quantitatively determined values from the entire powder sample are consistent with the TEM images in Figure S1. Due to the large size of the nanoplates, DSE refinement was not run against the neutron PDF data. Similar strategies have been applied to the DSE refinement of the morphology of the 500 °C calcined nanoplate sample. The average width is refined to be 38.4(8) nm, and the thickness is refined to be 17.9(5) nm. The refinement results are shown in Figure S13, Table S4, and Table 2.

**Table 2. Atomistic Structure and Morphology of {001} Dominant Anatase $TiO_2$ Nanoplates Refined from Powder XRD Data Using the Combined Differential Evolution and Least-Square Refinement with Monodisperse Model[a]**

| Atom | Wyck. | $x$ | $y$ | $z$ | Occ. | $B_{eq}$ (Å$^2$) |
|---|---|---|---|---|---|---|
| Ti | 2a | 0.00 | 0.25 | 0.375 | 1.0 | 0.45 |
| O | 4f | 0.00 | 0.25 | 0.1688 | 1.0 | 0.85 |

[a]Width ($w$) = 33.1 (11) nm; thickness ($h$) = 9.7 (3) nm. S.G. $I4_1/amd$ (2); $a$ = 3.7918 (4) Å; $c$ = 9.5019 (15) Å.

**Influence of Polydispersity on the Morphology Analysis of {001} Dominant Anatase $TiO_2$ Nanoplates.** Though tremendous efforts have been spent on pursuing monodispersed anatase $TiO_2$ nanocrystals in the last few decades,[6,14,53] an effective synthetic method has not been fully achieved yet, especially for nanocrystals with dominant highly energetic {001} facets.[49] Therefore, polydispersity should be taken into consideration for accurate morphology evaluation. While the Fourier analysis of Bragg diffraction profiles have been widely used to extract the polydispersity information out of powder diffraction data,[31,70,71] very few previous reports on polydispersity analysis using DSE can be found,[72−76] presumably due to the discrete nature of DSE calculation/refinement. This discrete nature means that only a numerical solution (not an analytical solution) can be used to extract the morphology distribution. For powder samples that contain large amounts of nanoparticles, it can be expected that the morphology varies nearly continuously from the smallest particle to the largest ones. Theoretically, the relationship between volumetric-based scattering power and the total scattering intensity ($I(Q)$) can be resolved if the morphology distribution function is known. This approach has been widely adapted for morphology analysis of small angle scattering data.[17,77] However, this method cannot provide any information about the atomistic structure because it utilizes a volumetric particle scattering factor instead of atomic scattering factors in calculating the total scattering intensity. Thus, the only method available to directly correlate both atomistic structure and morphology distribution to the total scattering intensity is the DSE calculation.

To numerically resolve the morphology distribution using DSE calculation, it is necessary to calculate X-ray diffraction patterns from a series of truncated anatase $TiO_2$ nano-octahedra with either fixed width ($w$) but variable thickness ($h$) or vice versa (grid points). After assigning a weighting scheme (number-based) to each calculated diffraction pattern (or grid), the morphology distribution can then be obtained by optimizing the weight of each calculated pattern using global minimization (preferred) or least-squares refinement until an


DOI: 10.1021/acs.chemmater.7b01172
Chem. Mater. XXXX, XXX, XXX−XXX

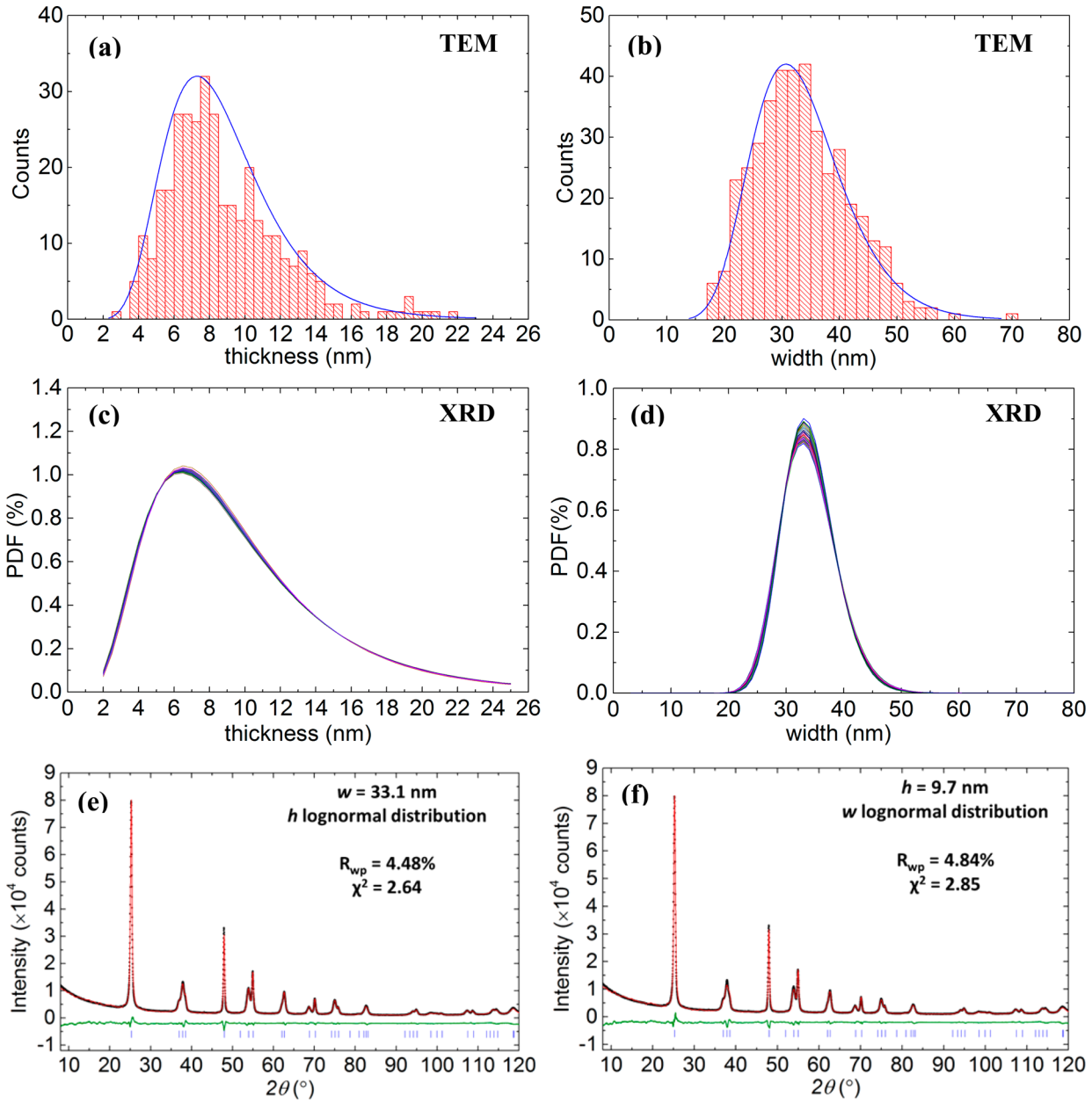


**Figure 8.** Thickness (a) and width (b) distribution of $TiO_2$ nanoplates (300 °C annealed) obtained from counting of TEM images. Blue curves are the log-normal fits of the observed distributions. Refined thickness (c) and width (d) distribution (number-based) of anatase $TiO_2$ nanoplate with XRD data (a population of 30 was chosen for the differential evolution refinement). Refinement results with thickness (e) and width (f) log-normal distribution. The calculated XRD patterns are shown in red, experimental data as black dots, and difference curves in green.

acceptable agreement between the calculated pattern and experimental data is achieved. Theoretically, it is possible to resolve both width and thickness distribution simultaneously. However, it is computationally too expensive to apply this to relatively large nanocrystals at this time. For example, if an interval of 1 nm is chosen for nanocrystals with thickness range of 25 nm and width range of 80 nm, a total of 2000 individual diffraction patterns have to be calculated. This is not practical for particles as large as tens of nanometers. In addition, no evidence of strong correlation between the plate thickness and width is observed from the TEM images (Figures S1–S3). Therefore, thickness and width distributions are refined separately (with either fixed width or fixed thickness). For width distribution refinement, the plate thickness was fixed to the average value of 9.7 nm while the width was allowed to vary from 5 to 80 nm with an interval of 1 nm; while for the thickness distribution refinement, the width was fixed to 33.1 nm while the thickness was varied from 1 to 26 nm with an interval of 0.5 nm. Both the width and the thickness are assumed to follow a log-normal distribution, which is found to be the most common polydispersity distribution for synthetic and natural nanoparticles.[78] It is also in general agreement with the TEM observations. The refinement results are shown in Figures 8c–f, and weighted refinement residuals are shown as a function of refinement generation in Figure S12. It can be seen that the mean thickness (8.6 nm) refined with the polydisperse model is much smaller relative to that refined from the monodisperse model (9.7 nm). The thickness of the prepared nanoplates is found to span a broad range with large standard deviation, a result that is fully consistent with the distribution


DOI: 10.1021/acs.chemmater.7b01172
Chem. Mater. XXXX, XXX, XXX–XXX

obtained from the counting of TEM images (Figure 8a). In contrast to the wide and asymmetrical distribution of the plate thickness, the refined plate width distribution behaves more symmetricly (close to Gaussian distribution) with smaller relative standard deviation. It is also worth noting that though the mean width (33.3 nm) obtained from TEM counting is similar to the refinement result, the distribution from TEM spans a slightly wider region relative to that obtained from the refinement. This can be understood by the fact that the average width of these nanoplates is large enough (over 30 nm) that the sensitivity from XRD is relatively low, as can be seen from the sensitivity test in Figure 1b. This is also reflected in the refinement result (Figure 8e,f), where the refinement of the thickness polydispersity improves the fits dramatically ($R_{wp}$ = 4.48%) while the refinement of the width polydispersity has only subtle improvements ($R_{wp}$ = 4.84%) relative to that of the refinement using the monodisperse model ($R_{wp}$ = 5.05%). These results demonstrate the importance of incorporating polydispersity for accurate morphology analysis and highlight challenges in the computational power required to do so. A similar strategy was applied to investigate the morphology polydispersity of the nano-octahedra and 500 °C calcined nanoplates, and the refined results are shown in Figure S15 and Figure S16. In contrast to the 300 °C calcined nanoplates sample, where the thickness polydispersity plays the major role, the width polydispersity was found to be the dominant effect for morphology polydispersity of these two samples.

The accuracy of the polydispersity fits to the three $TiO_2$ data were benchmarked against SANS analysis utilizing a disc model for the nanoplate samples and a sphere model for the nano-octahedra sample. Fits and solved polydispersity profiles of the disc and sphere diameters are shown in Figure S17. Direct modeling of the polydisperse nanoplate models were found most accurate when using the fixed thickness, varying width models. The resultant fits do not precisely correlate with the results of the DSE derived analysis and TEM counting, which suggests the average disc/sphere sizes are slightly smaller than the corresponding atomistic/counting models. The modeling of the nanoplates/octahedra as discs/sphere underestimates their surface area to volume ratio as compared to the true truncated octahedral nanostructures. In addition, while SANS is perhaps the most sensitive diffraction probe for particle size distributions, it cannot distinguish average particle size from average aggregate size. Models that are more sophisticated can be used to extrapolate more accurate morphology distribution profiles, which falls out of the scope of the current study and will be presented elsewhere.

**Quantitative Analysis of the Facet Dependent Photocatalytic Hydrogen Evolution Reactivity of Anatase $TiO_2$ Nanocrystals.** The anatase $TiO_2$ {001} facet with more undercoordinated $Ti_{5c}$ (five coordinated Ti) is generally believed to be more catalytically active relative to the energetically more stable {101} facet.[45] However, a number of controversial results have been reported in recent years where samples with higher percentages of {001} facets are found to be photocatalytically less active.[35,52] Several new theoretical models, such as the face-preferred surface charge carrier transfer[79] or the surface heterojunction,[80] are thus proposed to address the controversial observations. Nevertheless, a conclusive agreement has not been achieved, in large part due to the difficulty to fully separate and quantify the catalytic contributions from different facets, especially for nanocrystals with large surface areas for both facets. As has been discovered by Gordon et al.,[35] the measured BET surface of {001} dominant nanoplates is substantially smaller than the theoretical surface area calculated from morphology simulation due to significant particle stacking of nanoplates, as can be seen in Figure S1. This plate stacking significantly reduces the effective {001} surface but has negligible influence on the {101} surface. Therefore, simply normalizing the catalytic reaction rate to the BET surface often results in two possible mistakes: first, if the catalytic reaction is carried out using a well dispersed sample in liquids where much higher surface area is exposed (e.g., photohydrogenation using the methanol−water mixture) relative to the BET surface, it would result in the overestimation of the catalytic performance of the {001} dominant sample; second, if the catalytic reaction is carried out in powder form (such as $CO_2$ reduction), it would lead to the underestimation of the catalytic activity of {001} facets because of the serious plate stacking which heavily reduces the effective {001} surface area. Thus, in either case, it is highly desirable to calculate the accurate facet-specified surface areas to better understand the relationship between the catalytic performance and the morphology of anatase $TiO_2$ nanocrystals.

This inspired us to carry out the facet-specified surface area calculation for three nanocrystals with different {001} to {101} ratios: the {101} dominant nano-octahedra and {001} dominant nanoplates as described in the previous section, and a third sample with intermediate {001} to {101} ratio. The detailed calculation procedure for particle surface area is described in Figure S18. The calculation results using monodisperse thickness ($h$) and width ($w$) polydispersity models are shown in Figure S19 and Table S5. The theoretical surface area of the {001} dominant 300 °C annealed nanoplate is substantially higher than the corresponding BET surface. The {001} surface area calculated from thickness polydispersity (67.9 $m^2/g$) is significantly larger relative to the result obtained from the monodisperse model (46.7 $m^2/g$), indicating the importance of considering polydispersity for accurate surface area quantification. Interestingly, the surface areas calculated from width polydispersity are very similar to those obtained from the calculation of monodisperse models, which can be understood by the fact that the width distribution for the synthesized $TiO_2$ nanoplates is relatively narrow and symmetric (close to Gaussian distribution), as can be seen in Figure 8d. Similarly, the theoretical surface area of {101} dominant nano-octahedra calculated from a monodisperse model is also larger relative to the BET surface. However, this difference is very likely to arise from random particle aggregation instead of oriented stacking, as can be seen in the corresponding TEM images in Figure S1. Moreover, it is found that the width polydispersity (instead of thickness polydispersity) becomes the principal effect for the {101} dominant sample: the {101} surface area calculated from width polydispersity (137.8 $m^2/g$) is substantially larger relative to that obtained from the monodisperse model (106.2 $m^2/g$) while the {001} surface area only varies slightly from the monodisperse model. Similar character has been observed for the 500 °C calcined nanoplate sample, as can be seen in Table S5.

With the effective facet-specified surface area accurately determined, it is now possible to quantify the surface normalized photocatalytic hydrogen evolution reaction (HER) rate of anatase $TiO_2$ nanocrytals with different {001} to {101} ratios. After ultrasonic and under the vigorous photocatalysis stirring condition, it is expected that the stacking of $TiO_2$ nanocrystals is minimal so that the contact surface area


DOI: 10.1021/acs.chemmater.7b01172
Chem. Mater. XXXX, XXX, XXX−XXX

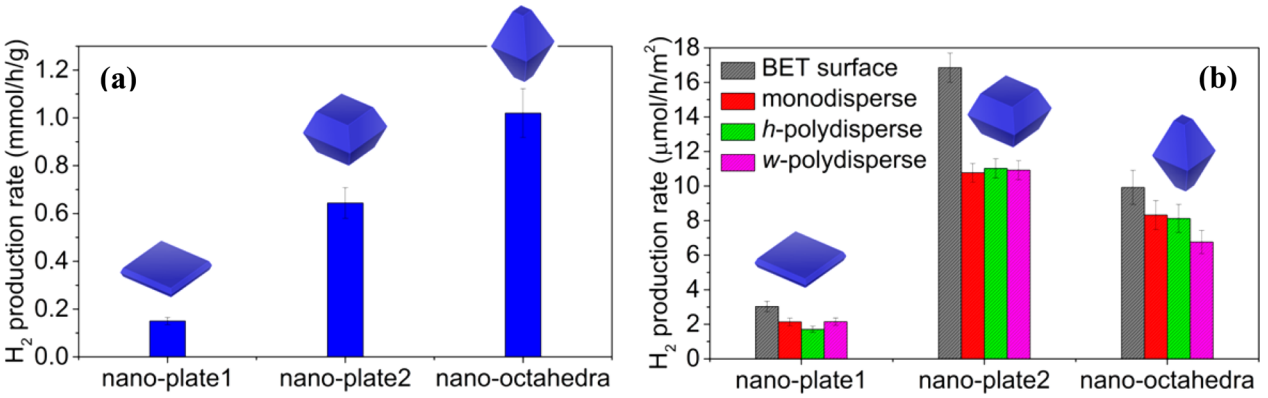


**Figure 9.** (a) Mass and (b) surface normalized photocatalytic HER of three anatase $TiO_2$ nanocrystals with different {001} to {101} facet ratios. Photocatalysis was conducted under UV irradiation (325−385 nm) with methanol as the sacrificial reagent. The apparent quantum yields (AQY) are 0.2% for nano-plate1 (300 °C), 1.7% for nano-plate2 (500 °C), and 2.1% for nano-octahedra.

should be close to the calculated theoretical surface area. The mass-normalized photocatalytic HER activities of the three anatase $TiO_2$ nanocrystals are shown in Figure 9 and Figure S20, which shows the HER activity rates in the order of nano-octahedra-300 °C > nanoplate-500 °C > nanoplate-300 °C. However, Figure 9 shows that the surface normalized HER rates follows the order of nanoplate-500 °C > nano-octahedra-300 °C ≫ nanoplate-300 °C. (The percentage of {001} facets follows the order of nanoplate-300 °C > nanoplate-500 °C ≫ nano-octahedra, contradicting previous assessments about the relative photocatalytic HER reactivity of {001} and {101} facets, where {001} facets are often simply reported to be either more or less[35,52] active relative to the {101} facets. Our observation clearly indicates that a high percentage of {001} facet (nanoplate-300 °C) does not guarantee better photocatalytic HER performance. Similarly, samples with a high percentage of {101} facet (nano-octahedra) show slower photocatalytic HER rate than the nanoplates with an intermediate fraction of both facets (nanoplate-500 °C), indicating that a high percentage of {101} facets alone also does not guarantee better photocatalytic HER performance. In fact, the nanocrystals with an intermediate percentage of both {001} and {101} facets shows the best surface normalized photocatalytic HER reactivity. This result suggests that synergistic effect may exist between {001} and {101} facets of anatase $TiO_2$, a phenomenon that has been recently observed by several groups though is based on a less quantitative analysis.[80−83] Therefore, our quantitative surface normalized activity analysis provides further evidence to support some of these assessments. It is also worth noting that the BET surface normalized HER activities are much higher relative to the theoretical surface normalized activities, reflecting the importance of accurate surface area calculation in avoiding overestimation of the hydrogen evolution rate from faceted anatase $TiO_2$ nanocrystals. Moreover, according to the previous report,[35,53] the residual surface $F^-$ can slightly increase (not decrease) the photocatalytic HER performance of nanoplate anatase $TiO_2$. Thus, the higher residual $F^-$ concentration in the 300 °C annealed nanoplate sample (relative to the other two samples, XPS in Figure S23) is unlikely to affect the current conclusion. Finally, it is worth noting that other factors, such as the population of point defects, the absolute particle size, the surface structure, and the capability to scatter/absorb light of different nanocrystals may also affect the photocatalytic activity.[35,84−86] Nevertheless, the current method to accurately determine the surface area normalized activity rate should still be applied to better underpin and understand these complex effects.

## CONCLUSION

Powder X-ray diffraction and neutron pair distribution function are demonstrated to be powerful tools to obtain both accurate average atomistic structure and morphology information on {001} and {101} faceted anatase $TiO_2$ nanocrystals. It is also demonstrated that the morphology (shape and size) distribution of anatase $TiO_2$ nanocrystals can be accurately determined through numerical analysis of powder diffraction data using the Debye scattering equation calculation. This method has been successfully used to quantify the facet-specified photocatalytic hydrogen evolution activity of anatase $TiO_2$ nanocrystals with different {001} to {101} ratios. It is found that the sample with an intermediate amount of both {001} and {101} facets shows the best photocatalytic HER activity. This result suggests that a synergistic effect may exist between {001} and {101} facets of anatase $TiO_2$ nanocrystals. It is expected that this morphology quantification technique could be generally adopted to study the relationship between morphology and functionality of other technological important nanomaterials.

## ASSOCIATED CONTENT

### Supporting Information

The Supporting Information is available free of charge on the ACS Publications website at DOI: 10.1021/acs.chemmater.7b01172.

TEM images, XRD patterns, simulated neutron PDF data, refinement scheme, morphology and structural parameter evolutions, refined polydispersity of nano-octahera and thicker nanoplates, fits of SANS data, surface area calculation, mass-normalized HER reactivity, technique details, and refinement macros (PDF)

## AUTHOR INFORMATION

**Corresponding Authors**

*(K.P.) E-mail: pagekl@ornl.gov.

*(J.L.) E-mail: liuj1@ornl.gov.

**ORCID**

Jue Liu: 0000-0002-4453-910X

Shuo Qian: 0000-0002-4842-828X

Beth S. Guiton: 0000-0002-9478-9190



DOI: 10.1021/acs.chemmater.7b01172
Chem. Mater. XXXX, XXX, XXX−XXX

Zili Wu: 0000-0002-4468-3240
Katharine Page: 0000-0002-9071-3383

## Notes

The authors declare no competing financial interest.

## ■ ACKNOWLEDGMENTS

This work was principally supported through the U.S. Department of Energy, Office of Science, Office of Basic Energy Sciences, Early Career Research Program, Award No. KC040602, under Contract No. DE-AC05-00OR22725. Research conducted at the NOMAD beamline at ORNL's Spallation Neutron Source and High Flux Isotope Reactor was sponsored by the Scientific User Facilities Division, Office of Basic Sciences, U.S. Department of Energy. Bio-SANS is operated by Center for Structural Molecular Biology (FWP-ERKP291), sponsored by DOE's Office of Biological and Environmental Research. Research at the 11-ID-B beamline used resources of the Advanced Photon Source, a U.S. Department of Energy (DOE) Office of Science User Facility operated for the DOE Office of Science by Argonne National Laboratory under Contract No. DE-AC02-06CH11357. Photocatalysis work was conducted at the Center for Nanophase Materials Sciences, which is a DOE Office of Science User Facility. Partial salary support (L.Y.) was provided by the National Science Foundation under OIA 1355438. Materials synthesis and laboratory characterization were supported by the U.S. Department of Energy, Office of Science, Basic Energy Sciences, Chemical Sciences, Geosciences, and Biosciences Division. This manuscript has been authored by UT-Battelle, LLC, under Contract No. DE-AC05-00OR22725 with the U.S. Department of Energy. The Department of Energy will provide public access to these results of federally sponsored research in accordance with the DOE Public Access Plan (http://energy.gov/downloads/doe-public-access-plan).

## ■ REFERENCES

(1) McEnaney, J. M.; Crompton, J. C.; Callejas, J. F.; Popczun, E. J.; Biacchi, A. J.; Lewis, N. S.; Schaak, R. E. Amorphous Molybdenum Phosphide Nanoparticles for Electrocatalytic Hydrogen Evolution. *Chem. Mater.* **2014**, *26*, 4826−4831.

(2) Bastus, N. G.; Merkoci, F.; Piella, J.; Puntes, V. Synthesis of Highly Monodisperse Citrate-Stabilized Silver Nanoparticles of up to 200 nm: Kinetic Control and Catalytic Properties. *Chem. Mater.* **2014**, *26*, 2836−2846.

(3) Zhou, G. M.; Wang, D. W.; Li, F.; Zhang, L. L.; Li, N.; Wu, Z. S.; Wen, L.; Lu, G. Q.; Cheng, H. M. Graphene-Wrapped $Fe_3O_4$ Anode Material with Improved Reversible Capacity and Cyclic Stability for Lithium Ion Batteries. *Chem. Mater.* **2010**, *22*, 5306−5313.

(4) Bruce, P. G.; Scrosati, B.; Tarascon, J. M. Nanomaterials for Rechargeable Lithium Batteries. *Angew. Chem., Int. Ed.* **2008**, *47*, 2930−2946.

(5) Chen, X.; Mao, S. S. Titanium Dioxide Nanomaterials: Synthesis, Properties, Modifications, and Applications. *Chem. Rev.* **2007**, *107*, 2891−2959.

(6) Liu, Y. D.; Tang, A. W.; Zhang, Q.; Yin, Y. D. Seed-Mediated Growth of Anatase $TiO_2$ Nanocrystals with Core-Antenna Structures for Enhanced Photocatalytic Activity. *J. Am. Chem. Soc.* **2015**, *137*, 11327−11339.

(7) Yang, H. G.; Sun, C. H.; Qiao, S. Z.; Zou, J.; Liu, G.; Smith, S. C.; Cheng, H. M.; Lu, G. Q. Anatase $TiO_2$ Single Crystals with A Large Percentage of Reactive Facets. *Nature* **2008**, *453*, 638−641.

(8) Sneed, B. T.; Young, A. P.; Jalalpoor, D.; Golden, M. C.; Mao, S. J.; Jiang, Y.; Wang, Y.; Tsung, C. K. Shaped Pd-Ni-Pt Core-Sandwich-Shell Nanoparticles: Influence of Ni Sandwich Layers on Catalytic Electrooxidations. *ACS Nano* **2014**, *8*, 7239−7250.

(9) Sun, S. B.; Yuan, D.; Xu, Y.; Wang, A. F.; Deng, Z. T. Ligand-Mediated Synthesis of Shape-Controlled Cesium Lead Halide Perovskite Nanocrystals via Reprecipitation Process at Room Temperature. *ACS Nano* **2016**, *10*, 3648−3657.

(10) Sohn, K.; Kim, F.; Pradel, K. C.; Wu, J. S.; Peng, Y.; Zhou, F. M.; Huang, J. X. Construction of Evolutionary Tree for Morphological Engineering of Nanoparticles. *ACS Nano* **2009**, *3*, 2191−2198.

(11) Tian, N.; Zhou, Z. Y.; Yu, N. F.; Wang, L. Y.; Sun, S. G. Direct Electrodeposition of Tetrahexahedral Pd Nanocrystals with High-Index Facets and High Catalytic Activity for Ethanol Electrooxidation. *J. Am. Chem. Soc.* **2010**, *132*, 7580−7581.

(12) Tian, N.; Zhou, Z. Y.; Sun, S. G.; Ding, Y.; Wang, Z. L. Synthesis of Tetrahexahedral Platinum Nanocrystals with High-Index Facets and High Electro-Oxidation Activity. *Science* **2007**, *316*, 732−735.

(13) Jun, Y. W.; Choi, J. S.; Cheon, J. Shape Control of Semiconductor and Metal Oxide Nanocrystals Through Non-hydrolytic Colloidal Routes. *Angew. Chem., Int. Ed.* **2006**, *45*, 3414−3439.

(14) Yin, Y.; Alivisatos, A. P. Colloidal Nanocrystal Synthesis and The Organic-Inorganic Interface. *Nature* **2005**, *437*, 664−670.

(15) Hua, X.; Liu, Z.; Bruce, P. G.; Grey, C. P. The Morphology of $TiO_2$ (B) Nanoparticles. *J. Am. Chem. Soc.* **2015**, *137*, 13612−13623.

(16) Andreev, Y. G.; Panchmatia, P. M.; Liu, Z.; Parker, S. C.; Islam, M. S.; Bruce, P. G. The Shape of $TiO_2$-B Nanoparticles. *J. Am. Chem. Soc.* **2014**, *136*, 6306−6312.

(17) Beaucage, G.; Kammler, H. K.; Pratsinis, S. E. Particle Size Distributions from Small-Angle Scattering Using Global Scattering Functions. *J. Appl. Crystallogr.* **2004**, *37*, 523−535.

(18) Iijima, S.; Ichihashi, T. Structural Instability of Ultrafine Particles of Metals. *Phys. Rev. Lett.* **1986**, *56*, 616−619.

(19) Ajayan, P. M.; Marks, L. D. Experimental-Evidence for Quasimelting in Small Particles. *Phys. Rev. Lett.* **1989**, *63*, 279−282.

(20) Maeda, K.; Takata, T.; Hara, M.; Saito, N.; Inoue, Y.; Kobayashi, H.; Domen, K. GaN: ZnO Solid Solution as A Photocatalyst for Visible-Light-Driven Overall Water Splitting. *J. Am. Chem. Soc.* **2005**, *127*, 8286−8287.

(21) Polking, M. J.; Han, M. G.; Yourdkhani, A.; Petkov, V.; Kisielowski, C. F.; Volkov, V. V.; Zhu, Y. M.; Caruntu, G.; Alivisatos, A. P.; Ramesh, R. Ferroelectric Order in Individual Nanometre-Scale Crystals. *Nat. Mater.* **2012**, *11*, 700−709.

(22) Rietveld, H. M. A Profile Refinement Method for Nuclear and Magnetic Structures. *J. Appl. Crystallogr.* **1969**, *2*, 65−71.

(23) Thompson, P.; Cox, D. E.; Hastings, J. B. Rietveld Refinement of Debye-Scherrer Synchrotron X-Ray Data from $Al_2O_3$. *J. Appl. Crystallogr.* **1987**, *20*, 79−83.

(24) Vondreele, R. B.; Jorgensen, J. D.; Windsor, C. G. Rietveld Refinement with Spallation Neutron Powder Diffraction Data. *J. Appl. Crystallogr.* **1982**, *15*, 581−589.

(25) Warren, B. E. *X-ray Diffraction*; Courier Corporation: 1969.

(26) Laue, M. V. Eine quantitative Prüfung der Theorie für die Interferenzerscheinungen bei Röntgenstrahlen. *Ann. Phys.* **1913**, *346*, 989−1002.

(27) Scherrer, P. Bestimmung der inneren Struktur und der Größe von Kolloidteilchen mittels Röntgenstrahlen. *Kolloidchemie Ein Lehrbuch*; Springer: 1912; pp 387−409.

(28) Langford, J. I.; Wilson, A. J. C. Scherrer after 60 Years - Survey and Some New Results in Determination of Crystallite Size. *J. Appl. Crystallogr.* **1978**, *11*, 102−113.

(29) Stokes, A.; Wilson, A. A method of calculating the integral breadths of Debye-Scherrer lines. *Mathematical Proceedings of the Cambridge Philosophical Society*; Cambridge University Press: 1942; pp 313−322.

(30) Warren, B.; Averbach, B. The Effect of Cold-Work Distortion on X-ray Patterns. *J. Appl. Phys.* **1950**, *21*, 595−599.

(31) Scardi, P.; Leoni, M. Whole Powder Pattern Modelling. *Acta Crystallogr., Sect. A: Found. Crystallogr.* **2002**, *58*, 190−200.

(32) Hall, B. D. Debye function analysis of structure in diffraction from nanometer-sized particles. *J. Appl. Phys.* **2000**, *87*, 1666−1675.



DOI: 10.1021/acs.chemmater.7b01172
*Chem. Mater.* XXXX, XXX, XXX−XXX

(33) Debye, P. Zerstreuung von röntgenstrahlen. *Ann. Phys.* **1915**, *351*, 809−823.
(34) Egami, T.; Billinge, S. J. *Underneath the Bragg Peaks: Structural Analysis of Complex Materials*; Elsevier: 2003; Vol. *16*.
(35) Gordon, T. R.; Cargnello, M.; Paik, T.; Mangolini, F.; Weber, R. T.; Fornasiero, P.; Murray, C. B. Nonaqueous Synthesis of $TiO_2$ Nanocrystals Using $TiF_4$ to Engineer Morphology, Oxygen Vacancy Concentration, and Photocatalytic Activity. *J. Am. Chem. Soc.* **2012**, *134*, 6751−6761.
(36) Bertolotti, F.; Dirin, D. N.; Ibáñez, M.; Krumeich, F.; Cervellino, A.; Frison, R.; Voznyy, O.; Sargent, E. H.; Kovalenko, M. V.; Guagliardi, A.; Masciocchi, N. Crystal Symmetry Breaking and Vacancies in Colloidal Lead Chalcogenide Quantum Dots. *Nat. Mater.* **2016**, *15*, 987−994.
(37) Shoemaker, D. P.; Li, J.; Seshadri, R. Unraveling Atomic Positions in An Oxide Spinel with Two Jahn− Teller Ions: Local Structure Investigation of $CuMn_2O_4$. *J. Am. Chem. Soc.* **2009**, *131*, 11450−11457.
(38) Page, K.; Stoltzfus, M. W.; Kim, Y.-I.; Proffen, T.; Woodward, P. M.; Cheetham, A. K.; Seshadri, R. Local Atomic Ordering in $BaTaO_2N$ Studied by Neutron Pair Distribution Function Analysis and Density Functional Theory. *Chem. Mater.* **2007**, *19*, 4037−4042.
(39) Page, K.; Hood, T. C.; Proffen, T.; Neder, R. B. Building and Refining Complete Nanoparticle Structures with Total Scattering Data. *J. Appl. Crystallogr.* **2011**, *44*, 327−336.
(40) Liu, J.; Huq, A.; Moorhead-Rosenberg, Z.; Manthiram, A.; Page, K. Nanoscale Ni/Mn Ordering in the High Voltage Spinel Cathode $LiNi_{0.5}Mn_{1.5}O_4$. *Chem. Mater.* **2016**, *28*, 6817−6821.
(41) Farrow, C. L.; Billinge, S. J. L. Relationship between the atomic pair distribution function and small-angle scattering: implications for modeling of nanoparticles. *Acta Crystallogr., Sect. A: Found. Crystallogr.* **2009**, *65*, 232−239.
(42) Cargill, G. S. Influence of Neglected Small-Angle Scattering in Radial Distribution Function Analysis. *J. Appl. Crystallogr.* **1971**, *4*, 277−283.
(43) Olds, D.; Wang, H. W.; Page, K. DShaper: An Approach for Handling Missing Low-Q Data in Pair Distribution Function Analysis of Nanostructured Systems. *J. Appl. Crystallogr.* **2015**, *48*, 1651−1659.
(44) Fujishima, A.; Honda, K. Electrochemical Photolysis of Water at a Semiconductor Electrode. *Nature* **1972**, *238*, 37−38.
(45) Gong, X.-Q.; Selloni, A. Reactivity of Anatase $TiO_2$ Nanoparticles: the Role of the Minority (001) Surface. *J. Phys. Chem. B* **2005**, *109*, 19560−19562.
(46) Lazzeri, M.; Vittadini, A.; Selloni, A. Structure and Energetics of Stoichiometric $TiO_2$ Anatase Surfaces. *Phys. Rev. B: Condens. Matter Mater. Phys.* **2001**, *63*, 155409.
(47) Selloni, A. Crystal growth - Anatase shows its reactive side. *Nat. Mater.* **2008**, *7*, 613−615.
(48) Diebold, U. The Surface Science of Titanium Dioxide. *Surf. Sci. Rep.* **2003**, *48*, 53−229.
(49) Liu, S.; Yu, J.; Jaroniec, M. Anatase $TiO_2$ with Dominant High-Energy {001} Facets: Synthesis, Properties, and Applications. *Chem. Mater.* **2011**, *23*, 4085−4093.
(50) Han, X. G.; Kuang, Q.; Jin, M. S.; Xie, Z. X.; Zheng, L. S. Synthesis of Titania Nanosheets with a High Percentage of Exposed (001) Facets and Related Photocatalytic Properties. *J. Am. Chem. Soc.* **2009**, *131*, 3152−3153.
(51) Chen, J. S.; Tan, Y. L.; Li, C. M.; Cheah, Y. L.; Luan, D. Y.; Madhavi, S.; Boey, F. Y. C.; Archer, L. A.; Lou, X. W. Constructing Hierarchical Spheres from Large Ultrathin Anatase $TiO_2$ Nanosheets with Nearly 100% Exposed (001) Facets for Fast Reversible Lithium Storage. *J. Am. Chem. Soc.* **2010**, *132*, 6124−6130.
(52) Pan, J.; Liu, G.; Lu, G. M.; Cheng, H. M. On the True Photoreactivity Order of {001}, {010}, and {101} Facets of Anatase $TiO_2$ Crystals. *Angew. Chem., Int. Ed.* **2011**, *50*, 2133−2137.
(53) Liu, G.; Yang, H. G.; Pan, J.; Yang, Y. Q.; Lu, G. Q.; Cheng, H. M. Titanium Dioxide Crystals with Tailored Facets. *Chem. Rev.* **2014**, *114*, 9559−9612.
(54) Minella, M.; Faga, M. G.; Maurino, V.; Minero, C.; Pelizzetti, E.; Coluccia, S.; Martra, G. Effect of Fluorination on the Surface Properties of Titania P25 Powder: an FTIR Study. *Langmuir* **2010**, *26*, 2521−2527.
(55) Yang, X. H.; Li, Z.; Sun, C. H.; Yang, H. G.; Li, C. Z. Hydrothermal Stability of {001} Faceted Anatase $TiO_2$. *Chem. Mater.* **2011**, *23*, 3486−3494.
(56) Proffen, T.; Neder, R. B. DISCUS: A program for Diffuse Scattering and Defect-Structure Simulation. *J. Appl. Crystallogr.* **1997**, *30*, 171−175.
(57) Neuefeind, J.; Feygenson, M.; Carruth, J.; Hoffmann, R.; Chipley, K. K. The Nanoscale Ordered MAterials Diffractometer NOMAD at the Spallation Neutron Source SNS. *Nucl. Instrum. Methods Phys. Res., Sect. B* **2012**, *287*, 68−75.
(58) Coelho, A.; Chater, P.; Kern, A. Fast Synthesis and Refinement of the Atomic Pair Distribution Function. *J. Appl. Crystallogr.* **2015**, *48*, 869−875.
(59) Heller, W. T.; Urban, V. S.; Lynn, G. W.; Weiss, K. L.; O'Neill, H. M.; Pingali, S. V.; Qian, S.; Littrell, K. C.; Melnichenko, Y. B.; Buchanan, M. V.; Selby, D. L.; Wignall, G. D.; Butler, P. D.; Myles, D. A. The Bio-SANS instrument at the High Flux Isotope Reactor of Oak Ridge National Laboratory. *J. Appl. Crystallogr.* **2014**, *47*, 1238−1246.
(60) Arnold, O.; Bilheux, J.-C.; Borreguero, J.; Buts, A.; Campbell, S. I.; Chapon, L.; Doucet, M.; Draper, N.; Leal, R. F.; Gigg, M.; et al. Mantid—Data Analysis and Visualization Package for Neutron Scattering and $\mu$ SR Experiments. *Nucl. Instrum. Methods Phys. Res., Sect. A* **2014**, *764*, 156−166.
(61) Ilavsky, J.; Jemian, P. R. Irena: Tool Suite for Modeling and Analysis of Small-Angle Scattering. *J. Appl. Crystallogr.* **2009**, *42*, 347−353.
(62) Moore, P. B. Small-Angle Scattering - Information-Content and Error Analysis. *J. Appl. Crystallogr.* **1980**, *13*, 168−175.
(63) Olds, D. P.; Duxbury, P. M. Efficient Algorithms for Calculating Small-Angle Scattering from Large Model Structures. *J. Appl. Crystallogr.* **2014**, *47*, 1077−1086.
(64) Schneider, C. A.; Rasband, W. S.; Eliceiri, K. W. NIH Image to ImageJ: 25 Years of Image Analysis. *Nat. Methods* **2012**, *9*, 671−675.
(65) Barnard, A. S.; Curtiss, L. A. Prediction of $TiO_2$ Nanoparticle Phase and Shape Transitions Controlled by Surface Chemistry. *Nano Lett.* **2005**, *5*, 1261−1266.
(66) Williamson, G. K.; Hall, W. H. X-Ray Line Broadening from Filed Aluminium and Wolfram. *Acta Metall.* **1953**, *1*, 22−31.
(67) Cheary, R. W.; Coelho, A. A Fundamental Parameters Approach to X-Ray Line-Profile Fitting. *J. Appl. Crystallogr.* **1992**, *25*, 109−121.
(68) Petkov, V.; Cozzoli, P. D.; Buonsanti, R.; Cingolani, R.; Ren, Y. Size, Shape, and Internal Atomic Ordering of Nanocrystals by Atomic Pair Distribution Functions: A Comparative Study of $\gamma$-$Fe_2O_3$ Nanosized Spheres and Tetrapods. *J. Am. Chem. Soc.* **2009**, *131*, 14264−14266.
(69) Storn, R.; Price, K. Differential Evolution - A Simple and Efficient Heuristic for Global Optimization over Continuous Spaces. *J. Global Optim.* **1997**, *11*, 341−359.
(70) Scardi, P.; Leoni, M. Diffraction Line Profiles from Polydisperse Crystalline Systems. *Acta Crystallogr., Sect. A: Found. Crystallogr.* **2001**, *57*, 604−613.
(71) Kril, C. E.; Birringer, R. Estimating Grain-Size Distributions in Nanocrystalline Materials from X-ray Diffraction Profile Analysis. *Philos. Mag. A* **1998**, *77*, 621−640.
(72) Bertolotti, F.; Moscheni, D.; Migliori, A.; Zacchini, S.; Cervellino, A.; Guagliardi, A.; Masciocchi, N. A Total Scattering Debye Function Analysis Study of Faulted Pt Nanocrystals Embedded in A Porous Matrix. *Acta Crystallogr., Sect. A: Found. Adv.* **2016**, *72*, 632−644.
(73) Longo, A.; Sciortino, L.; Giannici, F.; Martorana, A. Crossing the Boundary Between Face-Centred Cubic and Hhexagonal Close Packed: the Structure of Nanosized Cobalt is Unraveled by A Model Accounting for Shape, Size Distribution and Stacking Faults, Allowing Simulation of XRD, XANES and EXAFS. *J. Appl. Crystallogr.* **2014**, *47*, 1562−1568.


DOI: 10.1021/acs.chemmater.7b01172
*Chem. Mater.* XXXX, XXX, XXX−XXX

(74) Cervellino, A.; Frison, R.; Bertolotti, F.; Guagliardi, A. DEBUSSY 2.0: the New Release of a Debye User System for NanoCrystalline and/or Disordered Materials. *J. Appl. Crystallogr.* **2015**, *48*, 2026−2032.
(75) Cervellino, A.; Giannini, C.; Guagliardi, A. DEBUSSY: a Debye User System for Nanocrystalline Materials. *J. Appl. Crystallogr.* **2010**, *43*, 1543−1547.
(76) Frison, R.; Cernuto, G.; Cervellino, A.; Zaharko, O.; Colonna, G. M.; Guagliardi, A.; Masciocchi, N. Magnetite−Maghemite Nanoparticles in the 5−15 nm Range: Correlating the Core−Shell Composition and the Surface Structure to the Magnetic Properties. A Total Scattering Study. *Chem. Mater.* **2013**, *25*, 4820−4827.
(77) Kammler, H. K.; Beaucage, G.; Mueller, R.; Pratsinis, S. E. Structure of Flame-Made Silica Nanoparticles by Ultra-Small-Angle X-ray Scattering. *Langmuir* **2004**, *20*, 1915−1921.
(78) Kiss, L. B.; Soderlund, J.; Niklasson, G. A.; Granqvist, C. G. The Real Origin of Lognormal Size Distributions of Nanoparticles in Vapor Growth Processes. *Nanostruct. Mater.* **1999**, *12*, 327−332.
(79) Tachikawa, T.; Yamashita, S.; Majima, T. Evidence for Crystal-Face-Dependent $TiO_2$ Photocatalysis from Single-Molecule Imaging and Kinetic Analysis. *J. Am. Chem. Soc.* **2011**, *133*, 7197−7204.
(80) Yu, J. G.; Low, J. X.; Xiao, W.; Zhou, P.; Jaroniec, M. Enhanced Photocatalytic $CO_2$-Reduction Activity of Anatase $TiO_2$ by Coexposed {001} and {101} Facets. *J. Am. Chem. Soc.* **2014**, *136*, 8839−8842.
(81) Liu, X. G.; Dong, G. J.; Li, S. P.; Lu, G. X.; Bi, Y. P. Direct Observation of Charge Separation on Anatase $TiO_2$ Crystals with Selectively Etched {001} Facets. *J. Am. Chem. Soc.* **2016**, *138*, 2917−2920.
(82) Liu, L.; Jiang, Y.; Zhao, H.; Chen, J.; Cheng, J.; Yang, K.; Li, Y. Engineering Coexposed {001} and {101} Facets in Oxygen-Deficient $TiO_2$ Nanocrystals for Enhanced $CO_2$ Photoreduction Under Visible Light. *ACS Catal.* **2016**, *6*, 1097−1108.
(83) Xiong, Z.; Luo, Y.; Zhao, Y.; Zhang, J.; Zheng, C.; Wu, J. C. Synthesis, Characterization and Enhanced Photocatalytic $CO_2$ Reduction Activity of Graphene Supported $TiO_2$ Nanocrystals with Coexposed {001} and {101} Facets. *Phys. Chem. Chem. Phys.* **2016**, *18*, 13186−13195.
(84) Wenderich, K.; Mul, G. Methods, Mechanism, and Applications of Photodeposition in Photocatalysis: A Review. *Chem. Rev.* **2016**, *116*, 14587−14619.
(85) Zhou, P.; Zhang, H.; Ji, H.; Ma, W.; Chen, C.; Zhao, J. Modulating the Photocatalytic Redox Preferences between Anatase $TiO_2$ {001} and {101} Surfaces. *Chem. Commun.* **2017**, *53*, 787−790.
(86) Kim, C. W.; Yeob, S. J.; Cheng, H.-M.; Kang, Y. S. A Selectively Exposed Crystal Facet-Engineered $TiO_2$ Thin Film Photoanode for the Higher Performance of the Photoelectrochemical Water Splitting Reaction. *Energy Environ. Sci.* **2015**, *8*, 3646−3653.


DOI: 10.1021/acs.chemmater.7b01172
*Chem. Mater.* XXXX, XXX, XXX−XXX